Journal of Magnetism and Magnetic Materials 321 (2009) 3653–3657

Contents lists available at ScienceDirect

Journal of Magnetism and Magnetic Materials

journal homepage: www.elsevier.com/locate/jmmm

# Magnetic order in $CaMn_2Sb_2$ studied via powder neutron diffraction

C.A. Bridges [a,*], V.V. Krishnamurthy [a], S. Poulton [b,c], M.P. Paranthaman [a], B.C. Sales [d], C. Myers [e], S. Bobev [e]

[a] Chemical Sciences Division, Oak Ridge National Laboratory, Oak Ridge, TN 37831 6100, USA
[b] NIST Center for Neutron Research, National Institute of Standards and Technology, Gaithersburg, MD 20899 8562, USA
[c] Department of Materials Science and Engineering, University of Maryland, College Park, MD 20742, USA
[d] Materials Science and Technology Division, Oak Ridge National Laboratory, Oak Ridge, TN 37831 6056, USA
[e] Department of Chemistry, University of Delaware, Newark, DE 19716, USA

ARTICLE INFO

*Article history:*
Received 30 September 2008
Received in revised form
19 June 2009
Available online 18 July 2009

*PACS:*
75.25.+z
75.30.Cr
75.50.Ee

*Keywords:*
Polar
Intermetallic
Magnetic structure
Representational analysis
Antiferromagnet
Neutron diffraction

ABSTRACT

This paper reports a neutron powder diffraction study of $CaMn_2Sb_2$ in the temperature range of 20–300 K. Collinear long-range antiferromagnetic order of manganese ions occurs below 85 K, where a transition is observed in the dc magnetic susceptibility measured with a single crystal. Short-range magnetic order, characterized by a broad diffraction peak corresponding to a *d*-spacing of approximately 4 Å ($2\theta \approx 22^\circ$), is also observed above 20 K. The long-range antiferromagnetic order is indexed by the chemical unit cell, indicating a propagation vector $\mathbf{k} = (0\,0\,0)$, with a refined magnetic moment of 3.38 $\mu_B$ at 20 K. Two possible magnetic models have been identified, which differ in spin orientation for the two manganese ions with respect to the *ab* plane. The model with spins oriented at a $25 \pm 2^\circ$ angle relative to the *ab* plane gives an improved fit compared to the other model in which the spins are constrained to the *ab* plane. Representational analysis can account for a model involving a *c*-axis component only by the mixing of two irreducible representations.

Published by Elsevier B.V.

## 1. Introduction

The attention of the condensed matter community has recently been captivated by the reports on high-superconducting transition temperatures for the doped versions of $BaFe_2As_2$ ($ThCr_2Si_2$-type structure; space group $I4/mmm$, No. 139) and the structurally related oxygen-bearing LaFeAsO materials (ZrCuSiAs-type structure, space group $P4/nmm$, No. 129) [1–5]. Though ubiquitous, the tetragonal $ThCr_2Si_2$-type structure is not the only arrangement adopted by the transition-metal pnictides with the general formula $AM_2X_2$, when *A* is a divalent cation, *M* is a transition-metal and *X* is a pnictogen, i.e., P, As, Sb or Bi. Another common structure formed in these systems is that of the trigonal $CaAl_2Si_2$ (also known as anti-$La_2O_3$ or -$La_2O_2S$) structure type. A large number of compounds with both structures have already been studied [1], and the specifics of the chemical bonding analyzed [6–8]. These comprehensive treatments describe a notable trend, which is of relevance to many doping studies—the $ThCr_2Si_2$-type structure is realized for nearly all late d-metals (*M* = groups 8 through 11 elements), when *X* = P or As, while phases with the $CaAl_2Si_2$-type structure form only with the $d^0$, $d^5$ and $d^{10}$ metals [1]. Thus, it has been suggested that the valance electron concentration is the dominating factor for the preference of one structure over the other; however, the fine balance between the atomic sizes to achieve efficient packing cannot be neglected too. The latter point is demonstrated by the fact that the alkaline-earth metal antimonides of the late transition-metals, as a rule, do not crystallize with the $ThCr_2Si_2$-type structure. On the other hand, $BaMn_2Sb_2$ crystallizes in the $ThCr_2Si_2$-type structure, while the isoelectronic Mn-containing pnictides with the remainder of the divalent series $AMn_2Sb_2$ (*A* = Ca, Sr, Eu, and Yb) all order in the $CaAl_2Si_2$-type crystal structure (space group $P\bar{3}m1$, No. 164) [9]. In both cases, the structures feature corrugated layers, formally $[Mn_2Sb_2]^{2-}$, separated by non-magnetic $A^{2+}$ cations, which show interesting magnetic properties.

Previous studies on the first representative of this series, $CaMn_2Sb_2$, have suggested a magnetic transition occurring near 250 K [10]. An antiferromagnetic long-range order has been proposed on the basis of spin-polarized density functional theory (DFT) calculations [10]. The magnetic properties reported for other $CaMn_2Sb_2$-analogs also appear to be dominated by strong Mn–Mn interactions. For example, the trigonal symmetry and the

* Corresponding author.
*E-mail address:* bridgesca@ornl.gov (C.A. Bridges).

0304-8853/$ - see front matter Published by Elsevier B.V.
doi:10.1016/j.jmmm.2009.07.015

possibility for a geometric magnetic frustration have been suggested to play a role in the complex antiferromagnetic ordering below 53 K in the isostructural $SrMn_2P_2$ [11], and within the $[Mn_2Sb_2]^{2-}$ sheets of $EuMn_2P_2$, though the $Eu^{2+}$ sublattice orders antiferromagnetically below 16.5 K [12]. In the case of $YbMn_2Sb_2$, long-range antiferromagnetic ordering has been observed below 120 K [13]. With this paper, we focus our attention on the magnetic ground state of $CaMn_2Sb_2$ by discussing the results from variable temperature powder neutron diffraction studies. Evidence for a short-range order and long-range antiferromagnetic order is presented based on the neutron diffraction experiments, and is corroborated by dc magnetic susceptibility measurements performed on an oriented single crystal.

## 2. Experimental details

Single crystals of $CaMn_2Sb_2$ were prepared from Sn flux as described previously [10], and subsequently ground in an agate mortar and pestle. Powder neutron diffraction data were collected on the BT-1 diffractometer at the NIST Center for Neutron Research. A Cu(3 1 1) monochromator with 15′ collimation were used to measure at temperatures 20, 70, 120, 200, and 300 K. Rietveld refinements were carried out at all temperatures using the program Fullprof [14]. dc Magnetic susceptibility measurements were performed with a Quantum Design SQUID magnetometer, using an oriented single crystal from the same batch of sample as was used for collection of the neutron diffraction data.

## 3. Results and discussion

Fig. 1 displays the single crystal dc magnetic susceptibility $\chi$ measured with the applied field H parallel to the *c*-axis and for applied field parallel to the *ab* plane. $\chi$ measured for $H \| c$-axis shows a broad maximum in the range 170–240 K, with the moment varying little below 100 K. A larger moment is observed parallel to the *ab* plane, with a feature of antiferromagnetic order near 85 K. In addition to the step in $\chi$, a peak or a minimum at 85 K in the Fisher heat capacity, defined as $\delta(T\chi)/\delta T$ [15], is shown in the insets; these features indicate the onset of long-range antiferromagnetic order for both $H \| ab$ plane and $H \| c$-axis. This is significantly lower than the $T_N$ of 250 K proposed by Bobev et al., deduced from a broad peak in the dc magnetic susceptibility measured on a polycrystalline sample [10]. The single crystal data presented here suggest that the broad peak at higher temperature relates to short-range magnetic order (SRO). It is useful at this stage to consider that geometric frustration has been proposed to influence magnetic ordering in these $CaAl_2Si_2$-type phases. In a study comparing magnetic ordering in $ThCr_2Si_2$-type $BaMn_2P_2$ ($T_N$ well above room temperature) with $CaAl_2Si_2$-type $SrMn_2P_2$, ($T_N = 53$ K), Brock et al. showed that magnetic frustration causes the long-range antiferromagnetic order to occur at a far lower temperature in $SrMn_2P_2$, despite the expectation of similar Mn–P–Mn superexchange interactions in the two phases [11]. This is caused both by magnetic frustration between $[Mn_2P_2]^{2-}$ sheets related to the trigonal symmetry of the $CaAl_2Si_2$-type structure, as well as within the sheets due to the stacking of triangular layers to form the $[Mn_2P_2]^{2-}$ bilayer [11–12]. Such geometric frustration is not present in the $ThCr_2Si_2$-type structure. A similar comparison may be made between $BaMn_2As_2$ and $CaMn_2As_2$. Magnetic susceptibility measurements suggest a high-ordering temperature for $ThCr_2Si_2$-type $BaMn_2As_2$ [9], while $CaAl_2Si_2$-type $CaMn_2As_2$ exhibits the much lower $T_N$ (85 K) reported here. On the basis of geometric arguments, comparison with the related $[Mn_2P_2]^{2-}$ phases, and the observation of a relatively low $T_N$ for $CaMn_2As_2$, it is expected that frustration plays a significant role in the magnetic interactions of this system.

The crystal structure was refined (Fig. 2) according to the model of Bobev et al. [10]. Non-magnetic Sn flux remaining from the crystal growth was present with a mass fraction of $7.6 \pm 0.6\%$ according to Rietveld refinement. Results presented in Table 1 indicate a continuous increase in cell volume, $c/a$ ratio and *c*-axis length with increasing temperature. An anomalous decrease in the *a*-axis length with increasing temperature is observed

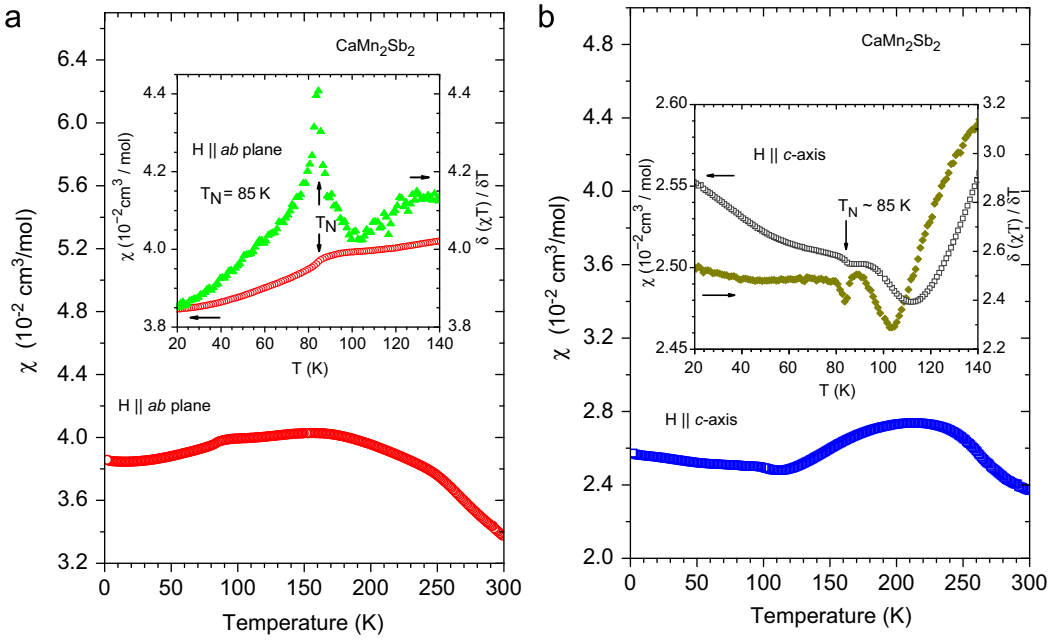


**Fig. 1.** Temperature dependence of dc magnetic susceptibility ($\chi$) on an oriented single crystal of $CaMn_2Sb_2$, measured in an applied field of 1 kOe in the field cooling cycle for (a) applied field $H \| ab$ plane and (b) $H \| c$-axis. Insets in (a) and (b) show the plot of $\chi$ and Fisher heat capacity $\delta(\chi T)/\delta T$ vs. temperature.

between 20 and 120 K, as was observed between 60 and 120 K in the isostructural phase $YbMn_2Sb_2$ [13]. The origin of the decrease in *a*-axis is unclear. While the temperature range over which it is observed may indicate a coupling between structural and magnetic ordering (magnetostrictive effect), further data are needed to confirm this possibility.

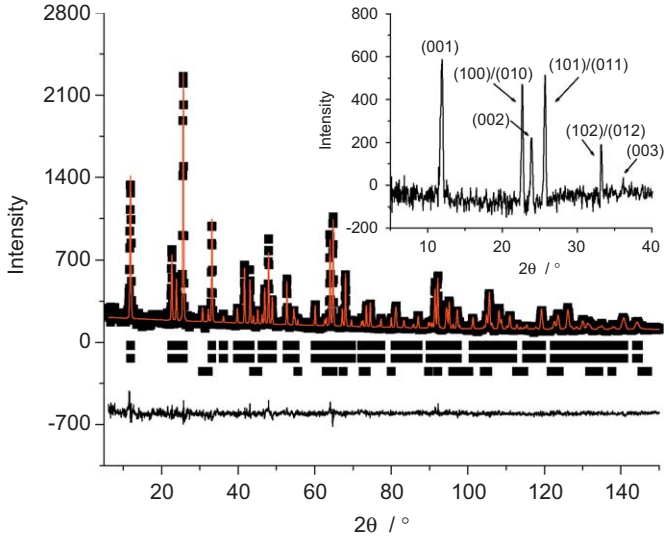


**Fig. 2.** Rietveld refinement of neutron powder diffraction data for $CaMn_2Sb_2$ collected at 20 K and $\lambda = 1.5403$ Å using model B (described in text). The upper vertical lines (reflection markers) correspond to the chemical structure, the middle to the magnetic structure (at identical positions to reflections from the chemical structure), and the lower reflection markers to the impurity phase, β-Sn. The inset displays the difference plot between 20 and 120 K data, with the indexing of magnetic reflections for the $\mathbf{k} = (0\,0\,0)$ magnetic cell given.

The low-angle paramagnetic scattering decreases significantly from 300 to 20 K (Fig. 3(a)). Magnetic reflections occur below 120 K, as shown in Fig. 3(b). Plots in Fig. 3(a) were obtained by subtracting the calculated (Rietveld refined) pattern, without a background correction, from the observed data at each temperature, thereby leaving the background together with some residual intensity at certain Bragg reflections; this was followed by smoothing of the data. A weak and broad peak centered near a *d*-spacing of ≈4 Å ($2\theta \approx 22^\circ$) is present due to SRO in 70, 120, and 200 K data, with a peak most clearly observed in 120 K data; the presence of this peak at 70 K indicates that short-range correlations persist into the long-range-ordered regime. A small component of this SRO may persist to 300 K, though this cannot be clearly shown with the available data. The counting time for each measurement was insufficient to give data of adequate quality to provide a detailed analysis of the short-range order here. However, it is useful to note that the nearest neighbour Mn–Mn distance is 3.18 Å, while the next-nearest neighbour distance is 4.53 Å, showing the broad peak does not correspond directly to a Mn–Mn correlation. This is near to the (1 0 0)/(0 1 0) reflection position at 3.92 Å, as well as the (0 0 2) reflection at 3.73 Å, suggesting that the broad peak could be related to magnetic correlations associated with these Bragg reflections. Despite some uncertainty in its characterization, it is expected that the broad, temperature-dependent maximum observed in the dc susceptibility (Fig. 1) corresponds to the presence of SRO.

Magnetic scattering intensity due to long-range order develops in reflection positions that can be indexed according to the

**Table 1**
Crystallographic and magnetic parameters[a].

| *T* (K) | *a* (Å) | *c* (Å) | *c*/*a* | *V* (Å)$^3$ | $z_{Mn}$ | $z_{Sb}$ | wRp | $\chi^2$ | $\mu_{Mn}$ ($\mu_B$) | Θ (°) | $R_{mag}$ |
|---|---|---|---|---|---|---|---|---|---|---|---|
| 300 | 4.5328 ± 0.0002 | 7.4870 ± 0.0004 | 1.6517 | 133.222 | 0.6216 ± 0.0007 | 0.2521 ± 0.0007 | 8.20 | 1.15 | – | – | – |
| 200 | 4.5272 ± 0.0001 | 7.4737 ± 0.0003 | 1.6508 | 132.654 | 0.6239 ± 0.0005 | 0.2517 ± 0.0005 | 7.84 | 1.03 | – | – | – |
| 120 | 4.5237 ± 0.0001 | 7.4622 ± 0.0003 | 1.6496 | 132.246 | 0.6235 ± 0.0005 | 0.2506 ± 0.0005 | 7.86 | 1.12 | – | – | – |
| 70 | 4.5249 ± 0.0001 | 7.4478 ± 0.0002 | 1.6460 | 132.060 | 0.6220 ± 0.0005 | 0.2503 ± 0.0005 | 7.89 | 1.09 | 2.91 ± 0.06 | Mn1 289 ± 3<br>Mn2 109 ± 3 | 9.75 |
| 20 | 4.5254 ± 0.0001 | 7.4428 ± 0.0002 | 1.6447 | 132.002 | 0.6221 ± 0.0005 | 0.2490 ± 0.0005 | 7.89 | 1.06 | 3.38 ± 0.06 | Mn1 295 ± 2<br>Mn2 115 ± 2 | 8.65 |

[a] Refinements at 20 and 70 K were conducted using model B (see text).

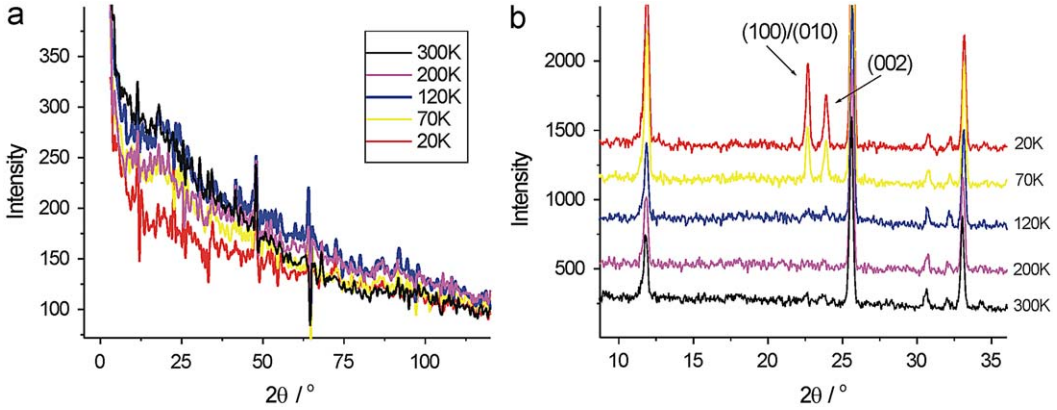


**Fig. 3.** Neutron powder diffraction data for $CaMn_2Sb_2$ indicating (a) the variation in background with temperature, showing the overall decrease in low-angle paramagnetic scattering with decreasing temperature (see text); (b) the onset of magnetic long-range order below 120 K. The (1 0 0)/(0 1 0) and (0 0 2) reflections near 24° 2θ are mainly magnetic in origin.

chemical cell, indicating a propagation vector (**k**) of (0 0 0). The magnetic representations corresponding to this propagation vector and the Mn 2d Wyckoff position are found to be $\Gamma_2$, $\Gamma_3$, $\Gamma_5$, and $\Gamma_6$ using the program SARAh [16], and are given in Table 2. The symmetry allowed structures correspond to collinear antiferromagnetic alignment along the *c*-axis ($\Gamma_2$) or in the *ab* plane ($\Gamma_6$), and collinear ferromagnetic alignment along the *c*-axis ($\Gamma_3$) or in the *ab* plane ($\Gamma_5$). We find that when utilizing a single representation, the best fit to the magnetic scattering intensity at 20 K is given by the $\psi_5$ basis vector of the $\Gamma_6$ representation, using a coefficient of 1.26 (wRp = 7.98; $\chi^2 = 1.08$; $R_{mag} = 8.87$). This corresponds to a moment of $3.25 \pm 0.06\,\mu_B$, with the moment vector aligned along a direction perpendicular to the *b*-axis and an antiparallel alignment of the Mn1 and Mn2 positions. In fact, the data can be equally well refined with the $\psi_6$ basis vector, which defines an orientation perpendicular to the $\psi_5$ basis vector, or any linear combination of the $\psi_5$ and $\psi_6$ basis vectors; there is insufficient information from data collected on a powder to define the orientation of the moments in the *ab* plane, so we may state simply that the $\Gamma_6$ representation provides the best fit to the data (model A) for an individual irreducible representation. This is displayed in Fig. 4.

**Table 2**
The basis functions ($\psi_n$) of the irreducible group representations of space group $P\bar{3}m1$, corresponding to the propagation vector **k** = (0 0 0).

| IR | Basis vector | Mn1 | | | Mn2 | | |
|---|---|---|---|---|---|---|---|
| | | $m_x$ | $m_y$ | $m_z$ | $m_x$ | $m_y$ | $m_z$ |
| $\Gamma_2$ | $\psi_1$ | 0 | 0 | 6 | 0 | 0 | −6 |
| $\Gamma_3$ | $\psi_2$ | 0 | 0 | 6 | 0 | 0 | 6 |
| $\Gamma_5$ | $\psi_3$ | 0 | −1.5 | 0 | 0 | −1.5 | 0 |
| | $\psi_4$ | −1.732 | −0.866 | 0 | −1.732 | −0.866 | 0 |
| $\Gamma_6$ | $\psi_5$ | 3 | 1.5 | 0 | −3 | −1.5 | 0 |
| | $\psi_6$ | 0 | −2.598 | 0 | 0 | 2.598 | 0 |

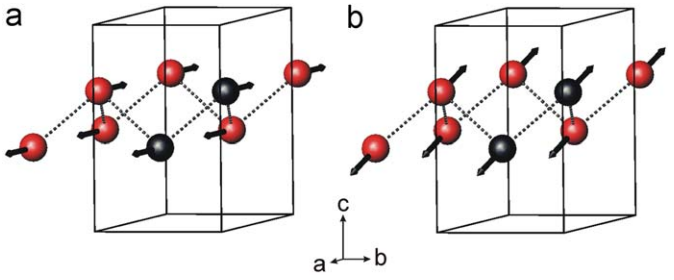


**Fig. 4.** Antiferromagnetic long-range-ordered structure of $CaMn_2Sb_2$ based upon (a) model A and (b) model B. The two Mn ions within the unit cell are labelled and displayed in black, while Mn ions outside the cell are in red. Mn1 and Mn2 are equivalent by symmetry in the chemical structure. Though the moment orientation is not defined in the *ab* plane by the available data, for both models the orientation of vectors is presented along the *a*-axis direction for clarity.

However, a slightly improved fit (wRp = 7.89; $\chi^2 = 1.06$; $R_{mag} = 8.65$) can be obtained using the magnetic structural model reported for $YbMn_2Sb_2$ [13], in which the spins lie predominantly along the *a*-axis, with a component along the *c*-axis, for a total moment of $3.38 \pm 0.06\,\mu_B$. The improved result (model B) must be considered with some care as the statistical improvement is minor. The final refinement in both cases involved all crystallographic and magnetic structural parameters given in Table 1, as well as isotropic atomic displacement parameters, background parameters, profile parameters, and a zero-point correction. We find that the slightly poorer fit for model A is not related to a problem in modelling the chemical structure; furthermore, there is no evidence from Rietveld refinement for a structural component to the phase transition at 85 K. The improved fit of model B is due to the additional *c*-axis component in the magnetic structure, adding one additional parameter for a total of 21 refined variables. It is well known that while the various Rietveld discrepancy values are useful indicators of the quality of fit, this must also be judged on the basis of a graphical assessment [17,18]. The difference in fit between the two models is most readily observed at the (0 1 0)/(1 0 1) reflection, near $2\theta = 22.67^\circ$. We can see in Fig. 5 that a small, but clear improvement is gained by the use of model B, corresponding to a tilting of $25 \pm 2^\circ$ away from the *ab* plane of the magnetic moment at 20 K. We therefore tentatively select this model as the appropriate magnetic structure. Model B has been used for the summary in Table 1. The spins have a parallel orientation within each Mn sublattice, with antiparallel orientation between sublattices; the magnetic order arises primarily from nearest neighbour Mn1–Mn2 antiferromagnetic coupling. This model agrees closely with the prediction of Bobev et al. in [10]. Though the spin-polarized DFT calculations could not predict the precise orientation of the spins, the calculated magnitude of the moment (in the range of 3.2–3.5 $\mu_B$) is in good agreement with the results reported here.

The technique of representational analysis involves the determination of magnetic modes by decomposing the magnetic representation $\Gamma$ of a space group $G_k$ into irreducible representations [19]. This procedure is based upon the Landau theory of a second-order phase transition, and states that at the ordering

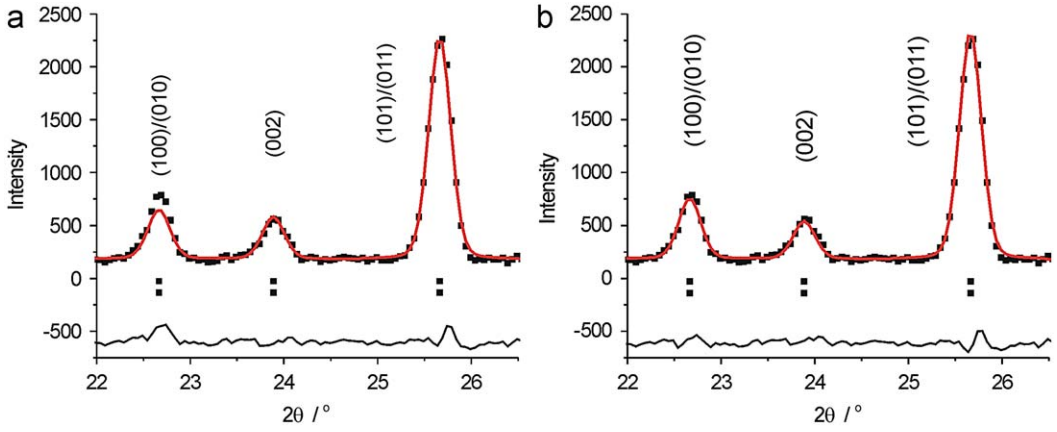


**Fig. 5.** Rietveld refinement of neutron powder diffraction data for $CaMn_2Sb_2$ collected at 20 K and $\lambda = 1.5403$ Å. The difference in the quality of the fit for (a) model A and (b) model B. The addition of a *c*-axis component to the magnetic moment improves the overall fit, but is particularly evident for the (1 0 0)/(0 1 0) reflection at $2\theta = 22.67^\circ$.

transition only one irreducible representation can become critical [20]. As model B can only be described using a combination of the $\Gamma_2$ and $\Gamma_6$ representations, this implies that there is first-order character to the magnetic phase transition. The requirement of more than one irreducible representation to describe a magnetic structure is well known, though it occurs relatively infrequently [21]. Another possibility exists to explain the apparent requirement of two irreducible representations to describe the magnetic structure: the two representations could become critical at two separate second-order phase transitions. While the powder neutron diffraction data do not provide any evidence for the existence of two transitions, these data alone are not sufficient to exclude this possibility experimentally; however, this scenario is not supported by the magnetic susceptibility data, which only show evidence for one transition in the Fisher heat capacity (Fig. 1). We expect that the preceding analysis of magnetic order in $CaMn_2Sb_2$ is directly relevant to magnetic order in the isostructural intermetallic compounds $YbMn_2Sb_2$ [13] and $SrMn_2Sb_2$ [10]. It would be useful to re-examine these other $d^5$ Mn-containing $CaAl_2Si_2$-type structures, as a similar relationship observed between magnetic order and crystal structure type is expected to be revealed on the basis of representational analysis.

## 4. Conclusion

A combination of single crystal dc magnetic susceptibility and powder neutron diffraction has been used to characterize long-range antiferromagnetic order in $CaMn_2Sb_2$ below 85 K. Short-range magnetic order has been observed experimentally above 20 K. A magnetic unit cell, equal in size to the chemical unit cell and containing two antiferromagnetically coupled Mn spins oriented at an angle of $25\pm2^\circ$ relative to the *ab* plane, has been tentatively assigned. A moment of $3.38\pm0.06\,\mu_B$ was determined. This result is in disagreement with the expectations of Landau theory for a single second-order phase transition, as applied to representational analysis.

## Acknowledgements

This research was sponsored by the Division of Materials Sciences and Engineering (DMSE), Office of Basic Energy Sciences, US Department of Energy under Contract no. DE-AC05-00OR22725 with Oak Ridge National Laboratory, managed by UT-Battelle, LLC. S. B. gratefully acknowledges funding from the University of Delaware and the Petroleum Research Fund (ACS-PRF). C. M. was financially supported by the 2007 NSF Summer Research Program in Solid State Chemistry.

*Commercial product disclaimer*: the identification of any commercial products or trade name does not imply endorsement or recommendation by the National Institute of Standards and Technology.

## References

[1] P. Villars, L.D. Calvert, Pearson's Handbook of Crystallographic Data for Intermetallic Compounds, second ed., American Society for Metals, Materials Park, Ohio, USA, 1991.
[2] Y. Kamihara, T. Watanabe, M. Hirano, H. Hosono, J. Am. Chem. Soc. 130 (2008) 3296.
[3] A.S. Sefat, R. Jin, M.A. McGuire, B.C. Sales, D.J. Singh, D. Mandrus, Phys. Rev. Lett. 101 (2008) 117004.
[4] M. Rotter, M. Tegel, D. Johrendt, I. Schellenberg, W. Hermes, R. Pöttgen, Phys. Rev. B 78 (2008) 20503.
[5] N. Ni, S.L. Bud'ko, A. Kreyssig, S. Nandi, G.E. Rustan, A.I. Goldman, S. Gupta, J.D. Corbett, A. Kracher, P.C. Canfield, Phys. Rev. B 79 (2008) 14507.
[6] J.K. Burdett, G.J. Miller, Chem. Mater. 2 (1990) 12.
[7] C. Zheng, R. Hoffmann, R. Nesper, H.-G. von Schnering, J. Am. Chem. Soc. 108 (1986) 1876.
[8] R. Hoffmann, C. Zheng, J. Phys. Chem. 89 (1985) 4175.
[9] S.-Q. Xia, C. Myers, S. Bobev, Eur. J. Inorg. Chem. (2008) 4262.
[10] S. Bobev, J. Merz, A. Lima, V. Fritsch, J.D. Thompson, J.L. Sarrao, M. Gillessen, R. Dronskowski, Inorg. Chem. 45 (2006) 4047.
[11] S.L. Brock, J.E. Greedan, S.M. Kauzlarich, J. Solid State Chem. 113 (1994) 303.
[12] A.C. Payne, A.E. Sprauve, M.M. Olmstead, S.M. Kauzlarich, J.Y. Chan, B.A. Reisner, J.W. Lynn, J. Solid State Chem. 163 (2002) 498.
[13] A.V. Morozkin, O. Isnard, P. Henry, S. Granovsky, R. Nirmala, P. Manfrinetti, J. Alloys Compd. 420 (2006) 34.
[14] J. Rodriguez-Carvajal, Physica B 192 (1993) 55.
[15] M.E. Fisher, Philos. Mag. 7 (1962) 1731.
[16] A.S. Wills, Physica B 276 (2000) 680.
[17] B.H. Toby, Powder Diffr. 21 (2006) 67.
[18] L.B. McCusker, R.B. Von Dreele, D.E. Cox, D. Louëjr, P. Scardi, J. Appl. Crystallogr. 32 (1999) 36.
[19] E.F. Bertaut, J. Magn. Magn. Mater. 24 (1981) 267.
[20] A.S. Wills, J. Mater. Chem. 15 (2005) 245.
[21] Y.u.A. Izyumov, V.E. Naish, S.B. Petrov, J. Magn. Magn. Mater. 13 (1979) 275.